Compact micromachined infrared bandpass filters for planetary spectroscopy

Willie C. Merrell, II Shahid Aslam, Ari D. Brown,* James A. Chervenak,
Wei-Chung Huang, Manuel Quijada, and Edward J. Wollack

NASA Goddard Space Flight Center, Greenbelt, Maryland 20771, USA

*Corresponding author: ari.d.brown@nasa.gov

The future needs of space-based, observational planetary and astronomy missions include low mass and small volume radiometric instruments that can operate in high-radiation and low-temperature environments. Here, we focus on a central spectroscopic component, the bandpass filter. We model the bandpass response of the filters to target the wavelength of the resonance peaks at 20, 40, and 60 μm and report good agreement between the modeled and measured response. We present a technique of using standard micromachining processes for semiconductor fabrication to make compact, free-standing, resonant, metal mesh filter arrays with silicon support frames. The process can be customized to include multiple detector array architectures, and the silicon frame provides lightweight mechanical support with low form factor.
OCIS codes: 040.2235, 040.1240, 120.2440, 220.4000.

1. Introduction

A new generation of filter radiometers and spectrometers is required for the investigation of the cold outer planets of the solar system and their icy moons [1]. The new instrumentation must operate in a cryogenic high-radiation environment, be lightweight, and show high radiometric signal to noise performance. For instance, the thermal instrument straw man payload on the proposed Europa Jupiter Orbiter [2], for surface emission mapping and measurement of thermal inertia of Europa in the 7 to 100 μm spectral wavelength range, calls for a mass budget of 3.7 kg and survival of a total ionizing dose of 2.9 Mrad [3,4]. Key optical components to such instruments are lightweight, radiation-hard, high-transmission bandpass filters which can be matched to cryogenic focal plane detector arrays for the far-mid IR spectral region.

One scheme for achieving high peak transmission coupled with the desired out-of-band attenuation can be realized through the use of multilayer arrays of cross-shaped or annular apertures in thin metal foils of films [5–8]. Square-shaped metal meshes and their complementary inverse structures have, respectively, inductive (high pass) and capacitive (low pass) responses to incident light [9]. Self-resonant elements can be realized by appropriately tailoring the mesh geometry to approximate a bandpass response. The filter response can also be tailored by incorporating appropriate delays between mesh layers. The inductive, capacitive, and resonant meshes are usually fabricated out of metal foils, which, in their simplest form, have a small thickness compared to the radiation wavelength. These can consist of structures, either freestanding or hot pressed into a dielectric media [7], in which the interlayer spacing, if present, is appropriately controlled. For spectral wavelengths >20 μm multilayer, noncrystalline dielectric filters are typically not suitable for applications which need high in-band transmissivity and high out-of-band rejection, because the required layer thickness results in high absorption by the dielectric [10]. Furthermore, it is unclear whether or not aging arising from exposure in high radiation environments will affect the mechanical strength and optical properties of the dielectric [11,12]. Also, in the high radiation environments encountered in spaceflight, one needs to

consider deep dielectric charging and spurious light generation due to high—energy-charged particles (e.g., cosmic rays) interacting with the dielectric volume. From this perspective, metallic (or metal-coated) structures are preferred over materials with low intrinsic conductivity, for use in future radiometric instruments for the outer planets.

The realization of metal mesh bandpass filters from commercial precision chemical milling and electroforming processes has a long and successful history in far-mid infrared astrophysics and remote sensing [11–16]. These precision-etched mesh examples, which consist of freestanding electroformed nickel sheets with a regular array of circular holes, are a variant on structures used as sorting sieves and printing screens. The screens described by Huggard et al. [16] were robust and showed high peak transmittance between 70 μm and 172 μm in spectral wavelength. Chen et al. [17] studied the effects of transmission of polarized light through cross-shaped holes with varying crossmember dimensions and fixed lattice constant. More recently, Melo et al. [18] successfully fabricated suspended resonant nickel metal mesh filters for discrete central wavelengths ranging from 30 μm to 750 μm using standard photolithographic techniques, and their measured transmission and bandwidths correlated well with the simulations from a 3D EM simulator.

Here, we demonstrate a technique of using standard micromachining processes for semiconductor fabrication to make compact, freestanding, resonant metal mesh bandpass filter arrays using silicon support structures. The filter and filter support structure architectures are customizable, which ensures their compatibility with compact cryogenic detector arrays used in state-of-the-art space instrumentation. By design, the silicon support structure is thermally matched to other elements of the micromachined detector and can be readily hybridized in practice. Silicon is lightweight, has a low form factor, and its mechanical support is robust in that it provides protection against deformation while handling and stacking the filters. The frame can also be used as a spacer for filter stacking or be extended to include baffles to prevent crosstalk between the detector channels. Using photolithography to make the frames also increases the fabrication throughput because multiple frame architectures can be produced on a single wafer.

Our fabrication technique also allows one to use a wide range of materials which are compatible with standard semiconductor fabrication processes. For instance, we choose copper as a radiation hard metallic material whose properties allow for low-loss operation in the desired wavebands. Furthermore, the use of copper filters on silicon frames allows us to remove nickel components present in the other technologies [18,19], which make them much more difficult to customize to the array format and are incompatible with superconducting and other magnetically sensitive sensors.

Our primary discussion will center on the fabrication of the filters on a silicon frame and characterizing their spectral bandpass response. As part of our design and characterization effort, we model the bandpass response of different filter element shapes to target peak transmittances at wavelengths of 20, 40, and 60 μm. The realized 20 μm filter exhibited unintended tapering and rounding of its edges, whose geometries can be approximated and inserted into our model. In all cases, we report good agreement with the modeled and measured bandpass response. We will also present a strategy for hybridizing the filter array with a sensor array for future integration into a far-mid IR spectrometer, photometer, or radiometer design.

This paper is organized as follows: In Section 2, we discuss the modeling of the filter response. In Section 3, we describe the fabrication of the filters. In Section 4, we discuss the transmission measurement of the filters and compare the results with the model. We provide a future outlook in Section 5 and conclude the paper in Section 6.

2. Filter Modeling

We desired a modeling framework capable of predicting resonant metal mesh filter response prior to fabrication, to help target specific passbands. For a review of the nature of the resonant metal mesh filter response, see [7]. The starting point for the modeling approach employed here follows the work of Porterfield et al. [20]. Specifically, we used the Ansys 3D electromagnetic solver HFSS to solve Maxwell's equations for a defined set of geometries and materials. For an infinite square tiling geometry, the mesh array was reduced by symmetry to a single unit cell with perfect electric and magnetic field boundary conditions, which are designated by E and H respectively in Fig. 1. Waveports were then placed on the top and bottom to facilitate the calculation of two port S parameters for light at normal incidence.

For hexagonal tiling geometries, we use the analysis technique described in [21]. Pairs of master and slave boundaries were placed to simulate an infinite array, and the excitation sources were two plane waves with orthogonal electric field polarizations as shown in Fig. 1. This approach allows the propagation properties of the structures to be studied as a function of the angle of incidence.

The material properties of the bulk metal in the filter were represented by a surface impedance approximation in the model. A bulk resistivity for the metal layer of 1.4×10^{-6} Ω cm was used in the simulated results. The dominant observed difference between this simple treatment and the Drude dielectric function derived from the data in Ordal et al. [22] within the filter passband is the magnitude of the computed absorption. The modeled ohmic component of the loss in the surface impedance model is 1.6% and is observed to increase by only ~30% in the Drude approximation at our frequencies.
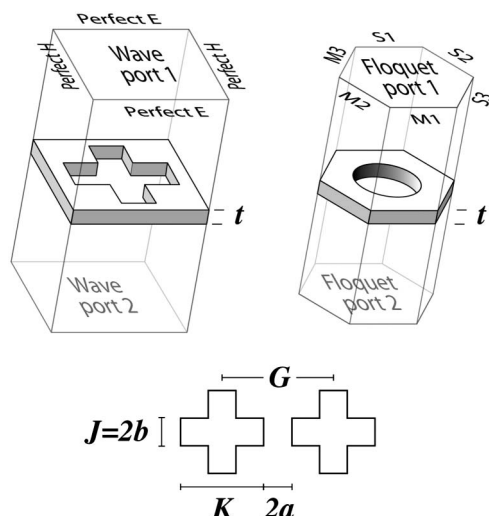
Fig. 1. Left: Modeling topology for the square tiling of crosses with perfect-E and perfect-H boundary conditions and thickness t. Right: Hexagonally close-packed circular filter with master boundaries (M1, M2, and M3), slave boundaries (S1, S2, and S3), and Floquet ports (F1 and F2). Bottom: The dimension parameters of the cross-shaped filter.

We modeled the filter material as a dielectric layer greater than the penetration depth in the metal at the lowest simulation frequency backed by a perfect-E surface [23]. This approach minimizes the required computing resources and provides reliable numerical results. The spectral resolution in the model was increased until the simulated response was observed not to change.

The location of the transmission response of a cross-shaped aperture, shown in Fig. 1, is determined by the periodicity, crossmember length, and crossmember width [20]. The filter profile can be scaled linearly by scaling the dimensions provided that the periodicity is smaller than the wavelength. In [24], Chase *et al.* define the dimensions of the structure differently, with the dimension b equal to half of the crossmember width and the dimension a equal to half of the difference of the periodicity and crossmember length. It was determined that the

resonant wavelength is approximately 2.1 times the crossmember length independent of a and b if the ratio of $b/a \leq 1$. Furthermore, the bandwidth increases as b/a increases; however, coupling between the crosses is also a significant factor in determining the bandwidth of the filter. Other aspects that influence the shape factor and characteristic of the filter include thickness of the metal as demonstrated in [25], the stacking or cascading of filters as demonstrated in [7,26], and the use of other shaped apertures [7,24,25,26]. The relations between the filter's dimensional parameters are indicated in Fig. 1.

3. Fabrication

Some examples of different array architectures of realized filters are shown in Fig. 2. Our fabrication process results in a freestanding copper resonant metal mesh filter suspended from a silicon support frame. In using MEMS fabrication techniques, we can achieve 1 μm alignment tolerance in delineating our filters, which is orders of magnitude better than assembly by hand.

The process starts (as shown in Fig. 3) by depositing a thermal oxide layer on both sides of 4" Si(001) wafers (resistivity ~10 to 20 Ω cm) using a tube furnace. The oxide serves as both an insulator, to prevent electroplating metal on the back of the wafer, and an etch stop for subsequent deep reactive ion etching. Front and back alignment marks are then patterned with a positive photoresist and reactive ion etched in $CF_4/Ar/CHF_3$ and SF_6/O_2 plasmas, in order to etch SiO_2 and Si, respectively. A sacrificial layer of commercially available Parylene-C (Specialty Coating Systems) is deposited onto the wafers and then patterned with positive photoresist. The Parylene is then etched in an O_2 plasma using a parallel plate barrel asher (Axic).

Parylene has several attractive features which make it a good sacrificial layer. It provides mechanical support and is easily removed in an O_2 plasma, which does not erode the copper mesh. We find that it is also compatible with the sulfuric acid based electroplating solution used to plate copper. This is
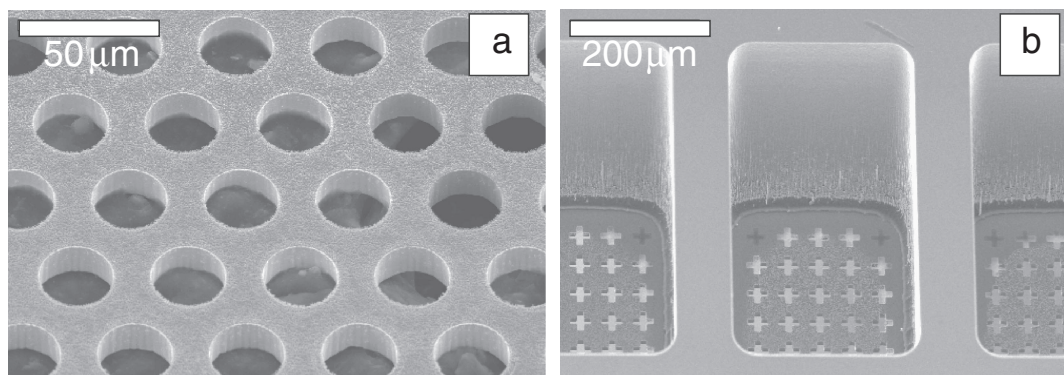

Fig. 2. (a) Scanning electron microscope (SEM) image of an electroplated copper mesh filter. The filter consists of a copper sheet with hexagonally close-packed circular holes. (b) SEM image of a linear filter array, in which each filter has cross-shaped holes. The dimensions of one aperture are 240 μm × 480 μm. Also visible in this image is the 400 μm thick silicon frame region which mechanically supports the filters. The apparent gaps between the silicon and copper are comprised of Parylene-C.

Thermally deposit oxide on both sides of Si wafer.

Pattern front and back alignment marks in SiO₂.

Coat wafer with Parylene sacrificial layer.

Pattern and etch Parylene.

Deposit Ti/Cu electroplating seed layer.

Pattern and etch electroplating mold.

Electroplate metal features.

Wax bond wafer to Pyrex wafer.

Pattern and etch (DRIE) backetch cut; reactive ion etch through oxide.

Etch away Parylene, exposed Ti/Cu seed layer metal, and slightly etch SU-8.

Release parts in acetone bath with ultrasonics if necessary.

Si

SiO₂

Parylene

Ti/Cu layer

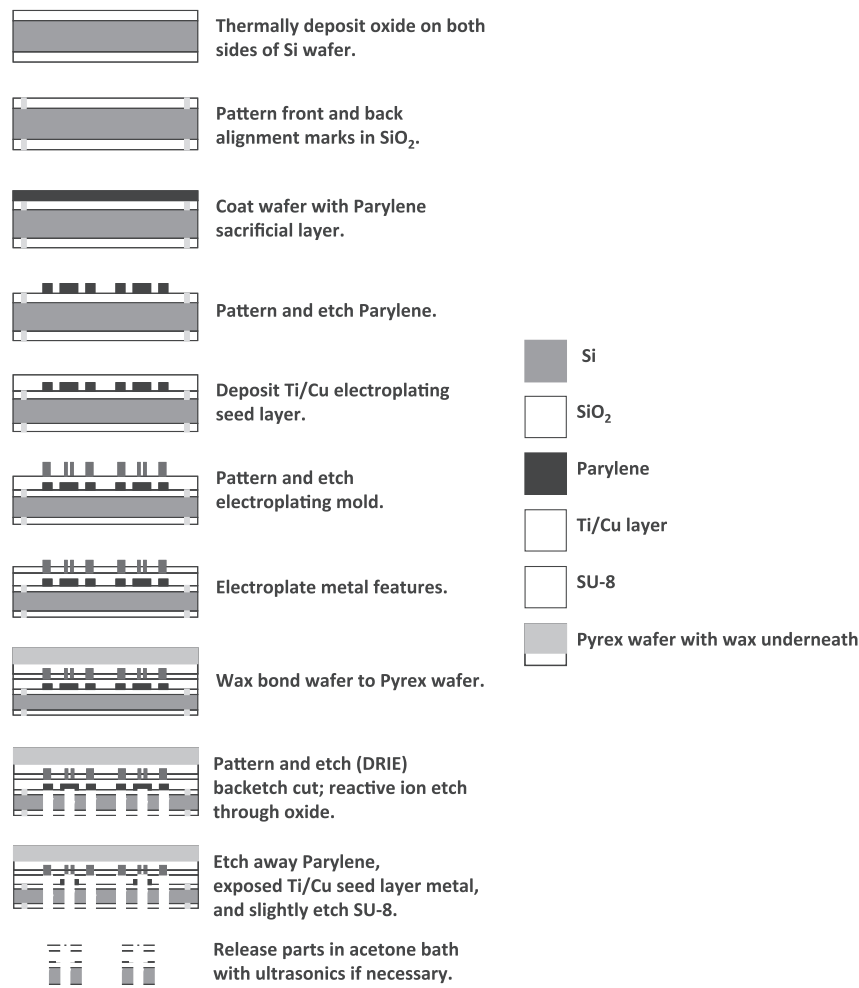SU-8

Pyrex wafer with wax underneath

Fig. 3.   Cross-section schematic diagram of the fabrication flow.

because it is both chemically inert (i.e., it does not dissolve in the solution) and is an insulator (i.e., plating does not occur on Parylene-coated surfaces). It also does not swell in aqueous solution; consequently, delamination of copper on Parylene surfaces is not a problem. Parylene has found previous use in space-flight missions [27] and has been demonstrated to be radiation hard [28]. The dielectric properties of Parylene are known to degrade with extended UV exposure [29]. However, as any residue remains outside of the optical path, this would have negligible influence on the electrical performance.

Following the patterning of the sacrificial layer, we electron beam deposited (base pressure = 2× 10⁻⁷ Torr) an electroplating seed layer which consisted of a 20 nm layer of Ti, which served as an adhesion layer between Cu and Parylene, and then a 200 nm layer of Cu at ambient temperature on the front side of the wafers. As an aside, we observed that the Ti/Cu seed layer results in a low-stress electroplated film [30]. The Cu surface was passivated by immersing the wafer in a 1:4000 benzotriazole:H₂O solution. The filter design was then patterned with SU-8-10 (Microchem) negative photoresist. Cu was

then electroplated in the SU-8—free regions using a sulfuric acid/copper sulfate based electroplating solution (Microfab-SC) and phosphorized copper anodes at ambient temperature. We found that in order to have smooth and near-vertical Cu sidewalls, the SU-8 thickness must exceed the Cu thickness. We have experience in patterning SU-8 with thicknesses ranging between 2 and 150 μm. For this work, the SU-8 thickness was 16 μm, which was more than sufficient for the 10 μm of electroplated Cu. The electroplated Cu was subsequently passivated in a benzotriazole solution.

In order to fabricate the silicon frame, we etched selected regions of the wafers from the backside. This consisted of bonding the front side of the wafers to Pyrex wafers using an acetone soluble wax (Crystalbond-509). We then ashed away the backside Parylene coating in an O₂ plasma and removed the backside oxide layer via reactive ion etching in a CF₄/Ar/CHF₃ plasma. The frame regions were defined using AZ-4620 positive photoresist and etched using an SF₆/O₂ etch and C₄F₈ passivation Bosch process in a deep reactive ion etcher (STS). We reactive ion etched the SiO₂ etch stop using a

$CF_4/Ar/CHF_3$ plasma, removed the Parylene in a parallel plate barrel asher with an O_2 plasma, stripped the Ti in $1:10$ $HF:H_2O$, and etched the Cu seed layer in a 1 M nitric acid solution. The remaining AZ-4620 resist was ashed away. Partial removal of the SU-8 was accomplished by ashing with an O_2/CF_4 plasma. Finally, the individual dice were released in an acetone bath and any remaining SU-8 was released in ultrasonic solvents.

In the event that the Cu surface was corroded post processing, the corrosion was removed in a 6% acetic acid solution and the Cu was passivated using a benzotriazole solution. This was found to protect the parts against subsequent corrosion after three months of exposure to atmosphere.

4. Transmission Measurement and Discussion

The transmission spectra were measured using a Bruker IFS 125 Fourier transform apectrometer (FTS). This instrument was equipped with a liquid helium–cooled bolometer that allowed us to collect data in the spectral range of $50–667$ cm^{-1} ($200–15$ μm) with a 0.5 cm^{-1} resolution. The data were taken in a focused beam configuration, with a focal number of 6.5, by taking the ratio of the filter transmission relative to a reference aperture. The low temperature measurements were taken using an Oxford Instruments liquid helium continuous flow optical cryostat mounted to the Bruker FTS. The circular reference aperture employed was 1.5 mm in diameter and the filters that were tested consisted of square-shaped mesh regions 1 mm on a side. A normalization factor computed from the ratio of the reference to the filter's area was applied to the measured transmission to correct for this effect.

The passbands were tuned by selecting the mesh hole geometry of the filter as discussed above. This facilitates making many filters of different passbands in a single fabrication run. For instance, we fabricated 19 dice, each with a different filter geometry, on a single 4" Si wafer. The resonance peaks of the passband are located close to the 20, 40, and 60 μm design targets. The transmittance at peak frequency for filters having cross-, square-, and circle-shaped holes is between 0.8 and 0.9 at 300 K as shown in Fig. 4. In general, the cross patterns give significantly narrower passbands and better long wavelength attenuation than the square or circle patterns. Furthermore, we note that the agreement between the modeled and measured transmittance is very good, and the transmittance results are comparable to other bandpass filters [18,19,31]. A standard means of improving filter bandwidth is to stack multiple filters [7]. Our models predict that stacking the filters will produce a sharper roll off and increased passband. A logical choice for a spacer between the filters is the silicon frame(s); other spacer materials which we have considered include epoxy loaded with polystyrene spheres and lithographically defined photoresist.
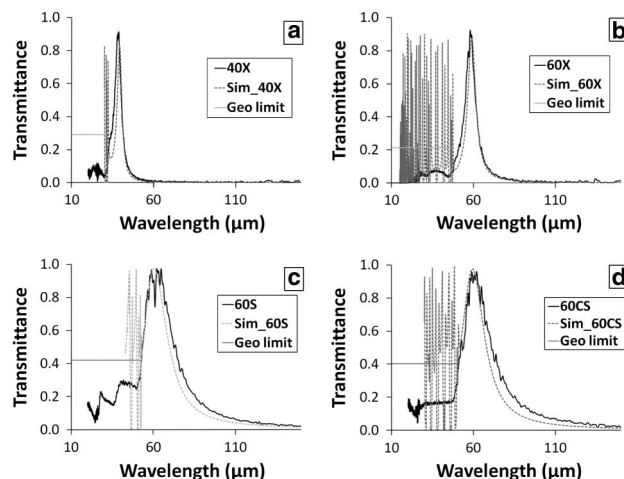

Fig. 4. FTS measurement of transmission spectra for a representative sampling of bandpass filters fabricated on a single 4" wafer. Shown in (a) and (b) are filters with cross-shaped holes, indicated by the X, arranged in a square lattice. (c) Filters with square holes, indicated by the S, arranged in a square lattice. (d) Circular holes with a hexagonally close packed lattice, indicated by CS. The number in the legend corresponds to the design peak frequency. The hole dimensions are (a) $G = 31.5$, $K = 20.5$, $J = 6$ μm; (b) $G = 47$, $K = 30.5$, $J = 9$ μm; (c) $G = 52.5$, $K = 34$ μm; and (d) $G = 58.5$, $K = 39$ μm. The measured mesh thickness is $t = 8$ μm. The horizontal line on each plot is the ratio of the aperture area over the unit cell area for each filter. This corresponds to transmittance in the geometric optics limit and agrees in magnitude with the average of the modeled transmittance. The observed structure in the modeled transmittance is expected at frequencies above the design band due to the excitation of higher order modes. These details are not observed in the measured data due to diffractive losses and the effective average over the finite angular acceptance by the focused beam in the FTS.

In addition to having good transmittance, our filters have a novel silicon frame which renders them much more compatible with mid and far IR pixelated cryogenic focal plane detector arrays than other mesh filters. This is because silicon is the most commonly used substrate for cryogenic focal plane detectors to make spectrometers and radiometers [32,33,34]. Consequently, a benefit of using filters with a silicon frame is that the ratio of the filter to detector pixel dimensions is independent of operating temperature. This, in turn, greatly facilitates filter to detector focal plane hybridization. A second important benefit of using a silicon frame is that it is diamagnetic (i.e., it has a very small magnetic moment). This is in contrast with a nickel frame, whose large magnetic moment can perturb the response of superconducting detectors, which include transition edge sensors [35]. As an aside, in order to validate its compatibility with operation at cryogenic temperature, we thermally cycled a filter ten times by submersion into liquid nitrogen and observed no change in its morphology. We also measured a slight increase in filter transmittance at liquid helium temperature.

Regardless of the frame material and architecture, we observe that there are limitations in the bandpass

response of metal mesh filters. This is anticipated from the underlying physics. In the limit where the wavelength λ is less than the periodicity of the tiling (i.e., $\lambda < 2G$ for a square lattice), an incident plane wave is scattered into higher order modes (e.g., a spectrum of plane waves). These modes are seen in the simulation as very narrow resonances in the transmittance outside the design passband. The peaks are absent from the FTS measurement for two reasons: (1) In using a focused beam, the measurement is averaged over a finite set of angles, and (2) power above the filter design band is diffracted by the filter outside the angle of acceptance of the FTS sensor. The horizontal line in each plot in Fig. 4 indicates the ratio of the open aperture area to the area of the unit cell. This is the transmittance expected in the geometric optics limit, which agrees with averaging over the modeled transmittance.

In addition to the presence of higher order modes transmitting through the filters, we encountered minor perturbations in the pattern geometry during filter fabrication. For instance, the cross- and square-shaped mesh hole features that were produced exhibit rounding at their corners that was not originally included in our simulations. This rounding occurred due to limitations in the method used to define small feature sizes during photolithographic processing. Guided by measurements of the mesh filter geometry, we simulated the approximate rounded and tapered holes (i.e., upper radius of ~ 2.5 μm and side-wall slope angle of ~ 6°), as shown in Fig. 5. Incorporation of these details improved the agreement between the observed transmission characteristics.

We can address this design and fabrication issue by improving lithographic capabilities so as to define smaller features. For instance, we found that SU-8 feature resolution can be enhanced by using a low pass filter (Omega Optical) during UV light exposure of the photoresist as shown in Fig. 6. This technique can push the feature size resolution to 2 μm. Furthermore, one can use lower throughput and much more costly techniques, such as electron beam lithography, to define features down to 0.1 μm. Another means to fabricate filters with very small hole dimensions

Fig. 6. (a) Micrograph of SU-8 posts without using a low pass filter during UV light exposure. (b) Picture of the SU-8 posts, in which the same lithography mask as in (a) was used with the inclusion of an SU-8 low pass filter (Omega Optical). The resulting structures are much more precisely defined.

would be to use a self-assembly technique, for instance, by using block copolymers [36] to fabricate an electroplating mask. In all instances, however, there is a penalty for using smaller features, namely a reduction in transmittance. Perhaps the most efficient means of eliminating such unwanted resonances is to integrate the metal mesh bandpass filter with an antireflection-coated crystal such as SrF_2, whose Restrahlen band would reject this spectral region by reflection.

5. Future Outlook

We envision integrating the filter array with a detector array to build a radiometer. The focal plane assembly consists of a thermopile array aligned with a filter array, and baffles separating the respective array elements to prevent detector crosstalk and reduce spurious signals arising from light reflected from the detectors. Low and high pass filter windows, which are supported by the same silicon frame, are placed in front of the filter array in order to remove the extra resonances from out-of-band response. An advantageous feature of the process described in this paper is that adding the extensions to make the baffles as features in the silicon frame is straightforward. In order to capture reflections off the detectors, the baffles need to be good absorbers. Some possible means of making baffles with high absorption involve using degenerately doped silicon wafers or
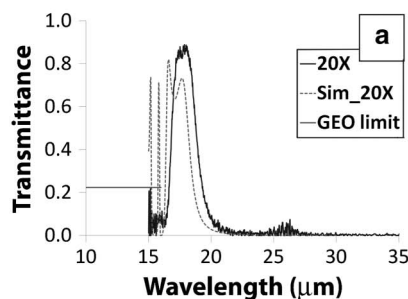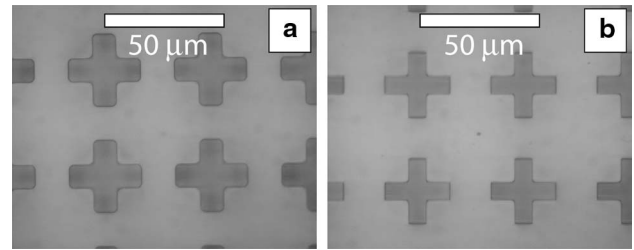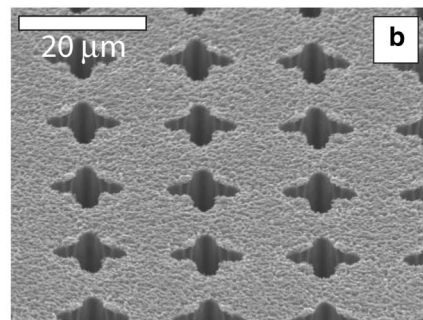

Fig. 5. (a) Shows the transmittance for the 20 μm cross-shaped filter. The scale has been changed to highlight the passband features. The realized geometry, which is a perturbation of the original design, exhibits rounding due to lithographic effects, shown in (b), which caused the filter bandpass response to deviate significantly from the initial modeled response. The included simulation of the bandpass response with rounded and tapered cross features gives improved agreement with measurement. The horizontal line in (a) is the ratio of the aperture area over the unit cell area for each filter.

coating the silicon with black anodized aluminum. We anticipate being able to satisfy mission requirements with custom designs of filter integration for a wide variety of radiometric instruments.

6. Conclusion

We have succeeded in making low mass, radiation hard, small volume, freestanding metal mesh filter arrays with silicon support frames, using standard semiconductor fabrication processes. The transmissivity is in the 0.8–0.9 range, and the measured bandpass response is in good agreement with the modeled response. The filter bandpass response contains more than one resonance, which was anticipated in the model. These additional resonances can be eliminated by fabricating much smaller features or by employing a low pass window with an antireflective coating. Our model results suggest we can maintain the necessary tolerance in stacking layers of these filters while improving the bandwidth and out-of-band rejection. The novel fabrication process that we present can also be extended to hybridize the filter array with the detector array so as to construct a compact and low profile radiometric instrument.

References and Notes

1. National Research Council, *Vision and Voyages for Planetary Science in the Decade 2013–2022* (National Academy, 2011).
2. NASA-ESA Report, Joint Science Definition Team, "Europa Jupiter System Mission—joint summary report," http://opfm.jpl.nasa.gov/library.
3. J. Boldt, "Overview of JEO model payload," presented at the Europa Jupiter System Mission 2nd Instrument Workshop, Baltimore, Maryland, 15–17 July 2009.
4. K. Clarke, T. Magner, and C. Erd, "Europa Jupiter Systems mission overview," presented at the Europa Jupiter System Mission 4th Instrument Workshop, Pasadena, California, 27–29 July 2010.
5. R. Ulrich, "Interference filters for the far infrared," Appl. Opt. **7**, 1987–1996 (1968).
6. V. Tomaselli, D. Edewaard, P. Gillan, and K. Möller, "Far-infrared bandpass filters from cross-shaped grids," Appl. Opt. **20**, 1361–1366 (1981).
7. P. Ade, G. Pisano, C. Tucker, and S. Weaver, "A review of metal mesh filters," Proc. SPIE **6275**, 62750U (2006).
8. P. Goldsmith, *Quasi-Optical Systems: Gausian Beam Quasioptical Propagation and Applications* (IEEE, 1998).
9. H. Booker, "Slot aerials and their relation to complementary wire aerials (Babinet's principle)," J. Inst. Elect. Eng. **93**, 620–626 (1946).
10. G. Holah, "Far-infrared and submillimeter-wavelength filters," in *Infrared and Millimeter Waves*, Vol. **6**, K. J. Button, ed. (Academic, 1982), pp. 305–409.
11. U. Akgun, P. Bruecken, A. Ayan, F. Duru, J. Olson, E. Albayrak, E. Gulmez, A. Mestvirishvili, Y. Onel, and I. Schmidt, "Radiation damage and light transmission studies on air core light guides," IEEE Trans. Nucl. Sci. **53**, 1547–1550 (2006).
12. G. Wang, G. Pan, L. Dou, R. Yu, T. Zhang, S. Jiang, and Q. Dai, "Proton beam modification of isotactic polypropylene," Nucl. Instrum. Methods Phys. Res. Sect. B **27**, 410–416 (1987).
13. K. Renk and L. Genzel, "Interference filters and Fabry–Perot interferometers for the far infrared," Appl. Opt. **1**, 643–648 (1962).
14. R. Rawcliffe and C. M. Randall, "Metal mesh interference filters for the far infrared," Appl. Opt. **6**, 1353–1358 (1967).
15. M. Dragovan, "Cryogenic metal mesh bandpass filters for submillimeter astronomy," Appl. Opt. **23**, 2798–2802 (1984).
16. P. Huggard, M. Meyringer, A. Schilz, K. Goller, and W. Prettl, "Far-infrared bandpass filters from perforated metal screens," Appl. Opt. **33**, 39–41 (1994).
17. C. Chen, M. Tsai, T. Chuang, Y. Tsung, and S. Lee, "Extraordinary transmission through a silver film perforated with cross shaped hole arrays in a square lattice," Appl. Phys. Lett. **91**, 063108 (2007).
18. A. Melo, M. Kornberg, P. Kaufmann, M. Piazzetta, E. Bortolucci, M. Zakia, O. Bauer, A. Poglitsch, and A. Alves da Silva, "Metal mesh resonant filters for terahertz frequencies," Appl. Opt. **47**, 6064–6069 (2008).
19. Lakeshore Cryotronics, Inc., "THz and far IR bandpass filters," http://www.lakeshore.com/products/THz-And-Far-IR-Band-Pass-Filters/Models/Pages/Overview.aspx.
20. D. Porterfield, J. Hesler, R. Densing, E. Mueller, T. Crowe, and R. Weikle, II, "Resonant metal-mesh bandpass filters for the far infrared," Appl. Opt. **33**, 6046–6052 (1994).
21. G. Pisano, P. Ade, and S. Weaver, "Polarization effects investigations in quasi-optical metal grid filters," Infrared Phys. Technol. **48**, 89–100 (2006).
22. M. Ordal, L. Long, R. Bell, S. Bell, R. Bell, R. Alexander, Jr., and C. Ward, "Optical properties of the metals Al, Co, Cu, Au, Fe, Pb, Ni, Pd, Pt, Ag, Ti, and W in the infrared and far infrared," Appl. Opt. **22**, 1099–1119 (1983).
23. E. Wollack, D. Fixsen, A. Kogut, M. Limon, P. Mirel, and J. Singal, "Radiometric waveguide calibrators," IEEE Trans. Instr. Meas. **56**, 2073–2078 (2007).
24. S. Chase and R. Joseph, "Resonant array bandpass filters for the far infrared," Appl. Opt. **22**, 1775–1779 (1983).
25. S. Kuznetsov, V. Kubarev, P. Kalinin, B. Goldenberg, V. Eliseev, E. Petrova, and N. Vinokurov, "Development of metal mesh based quasi-optical selective components and their applications in high-power experiments at Novosibirsk terahertz FEL," in *Proceedings of FEL 2007* (2007), pp. 89–92.
26. C. Winnewisser, F. Lewen, J. Weinzierl, and H. Helm, "Transmission features of frequency-selective components in the far infrared determined by terahertz time-domain spectroscopy," Appl. Opt. **38**, 3961–3967 (1999).
27. J. Iwanczyk, Y. Wang, J. Bradley, J. Conley, A. Albee, and T. Economou, "Performance and durability of HgI_2 X-ray detectors for space missions," IEEE Trans. Nucl. Sci. **36**, 841–845 (1989).
28. B. Patt, R. Dolin, T. Devore, J. Markakis, J. Iwanczyk, N. Dorri, and J. Trombka, "Radiation damage resistance in mercuric iodide X-ray detectors," Nucl. Instr. Meth. Phys. Res. A **299**, 176–181 (1990).
29. J. Fortin and T. Lu, "Ultraviolet radiation induced degradation of poly-para-xylylene (parylene) thin films," Thin Solid Films **397**, 223–228 (2001).
30. We also tried Ti/Au, Mo_2N, and TiN as seed layers. For Mo_2N and TiN, the electroplated film had poor adhesion to the substrate and Ti/Au had high surface roughness.
31. J. Adams, T. Herter, G. Gull, J. Schoenwald, C. Henderson, L. Keller, J. De Buizer, G. Stacey, and T. Nikola, "FORCAST: a first light facility instrument for SOFIA," Proc. SPIE **7735**, 77351U (2010).
32. N. Jethava, J. Chervenak, A. Brown, D. Benford, G. Kletetschka, V. Mikula, and K. U-yen, "Development of superconducting transition edge sensors based on electron-phonon decoupling," Proc. SPIE **7741**, 774120 (2010).
33. P. Mauskopf, P. Ade, J. Beyer, M. Bruijn, J. Gao, D. Glowaca, D. Goldie, D. Griffin, M. Griffin, F. Hoevers, P. Khosropanah,

P. Kooijma, P. De Korte, D. Morozov, A. Murphy, C. O'Sullivan, M. Ridder, N. Trappe, H. Van Weers, J. Van Der Kuur, and S. Withington, "TES focal plane for SPICA-SAFARI," in *Proceedings of the 21st International Symposium on Space Terahertz Technology* (National Radio Astronomy Observatory, 2010) pp. 246–255.

34. J. Wei, D. Olaya, B. Karasik, S. Pereverzev, A. Sergeev, and M. Gershenson, "Ultrasensitive hot-electron nanobolometers for terahertz astrophysics," Nat. Nanotechnol. **3**, 496–500 (2008).

35. K. Irwin and G. Hilton, "Transition edge sensors" in *Cryogenic Particle Detection*, C. Enss, ed. (Springer, 2005), pp. 63–149.

36. C. Tang, E. Lennon, G. Fredrickson, E. Kramer, and C. Hawker, "Evolution of block copolymer lithography to highly ordered square arrays," Science **322**, 429–432 (2008).